The Astrophysical Journal, 972:19 (12pp), 2024 September 1 https://doi.org/10.3847/1538-4357/ad5a89

Simultaneous Far-ultraviolet and Near-ultraviolet Observations of T Tauri Stars with UVIT/AstroSat: Probing the Accretion Process in Young Stars

Prasanta K. Nayak[1,2], Mayank Narang[1,3], P. Manoj[1], Uma Gorti[4,5], Annapurni Subramaniam[6], Nayana George[7], and Chayan Mondal[8]

[1] Department of Astronomy and Astrophysics, Tata Institute of Fundamental Research, Mumbai, 400005, India; nayakphy@gmail.com, pnayak@astro.puc.cl
[2] Instituto de Astrofísica, Pontificia Universidad Católica de Chile, Av. Vicuña MacKenna 4860, 7820436, Santiago, Chile
[3] Academia Sinica Institute of Astronomy & Astrophysics, 11F of Astro-Math Bldg., No.1, Sec. 4, Roosevelt Rd., Taipei 10617, Taiwan, R.O.C.
[4] NASA Ames Research Center, MS 245-3, Moffett Field, CA 94035, USA
[5] Carl Sagan Center, SETI Institute, Mountain View, CA 94043, USA
[6] Indian Institute of Astrophysics, Bangalore, 560034, India
[7] Cochin University of Science and Technology, India
[8] Inter-University Centre for Astronomy and Astrophysics, Pune, Maharashtra 411007, India
Received 2024 March 3; revised 2024 May 24; accepted 2024 June 14; published 2024 August 22

Abstract

We present results from simultaneous far-ultraviolet (FUV) and near-ultraviolet (NUV) observations of T Tauri stars (TTSs) in the Taurus molecular cloud with UVIT/AstroSat. This is the very first UVIT study of TTSs. From the spectral energy distribution of TTSs from FUV to IR, we show that classical TTSs (CTTSs) emit significantly higher UV excess compared to weak-line TTSs (WTTSs). The equivalent blackbody temperatures corresponding to the UV excess in CTTSs ($>10^4$ K) are also found to be relatively higher than those in WTTSs (<9250 K). From the UV excess, we have reclassified two WTTSs (BS Tau and V836 Tau) as CTTSs, which has been supported by the follow-up optical spectroscopic study using the Himalayan Chandra Telescope, showing strong Hα line emission. We find that CTTSs show strong excess emission in both the FUV ($>10^7$) and NUV ($>10^3$) bands, while WTTSs show strong excess only in the FUV ($\lesssim 10^5$), suggesting that excess emission in the NUV can be used as a tool to classify the TTSs. We also find a linear correlation between UV luminosity (a primary indicator of mass accretion) and Hα luminosity (a secondary indicator of mass accretion) with a slope of 1.20 ± 0.22 and intercept of 2.16 ± 0.70.

Unified Astronomy Thesaurus concepts: Pre-main sequence stars (1290); T Tauri stars (1681); Ultraviolet photometry (1740)

1. Introduction

T Tauri stars (TTSs) are low-mass pre-main-sequence stars, generally categorized into classical TTSs (CTTSs) and weak-line TTSs (WTTSs) based on their strength of Hα emission (Alcala et al. 1993; Duvert et al. 2000; Gras-Velázquez & Ray 2005). CTTSs show strong and broad Hα emission, indicating active ongoing accretion from the circumstellar disk onto the central star, while WTTSs show weak and narrow Hα emission, suggesting weak or no accretion (Herbig & Bell 1988; Martín 1998; Barrado y Navascués & Martín 2003; White & Basri 2003).

Circumstellar disks form during the process of star formation due to the conservation of angular momentum and in their short lifetimes (∼a few Myr) aid both star and planet formation. Material from the disk around the CTTS is channeled onto the stars along the strong magnetic field lines and generates accretion shocks on the stellar surface, producing hot spots (Hartmann et al. 2016, and references therein). The kinetic energy of the freely infalling material is dissipated in these accretion shocks. Behind these shocks, the energy is converted into radiation that flows back out through the shocks and into the infalling material. Most of the escaping radiation peaks in the ultraviolet with estimated blackbody equivalent temperatures of $\sim 10^4$ K (Calvet & Gullbring 1998). Thus, accreting stars are characterized by strong UV excesses (Gorti & Hollenbach 2009). The cool and dusty layers of the disk absorb this radiation and reemit at infrared wavelengths. Hence, the accretion process causes the release of excess energy not only in the UV but also in the IR regions of the spectral energy distribution (SED) of a CTTS. The UV emissions mainly originate from the hot spots produced by accretion shocks, while near-IR (NIR) and mid-IR emissions come from smaller disk radii and far-IR comes from the midplane of the outer disk. As the disk disperses, the SED gradually shows less excess in the IR region (Lada 1987). Nonaccreting WTTSs also show an excess in UV due to chromospheric activity and a significantly reduced excess in IR due to the presence of a smaller or depleted disk (Ingleby et al. 2011; Schneider et al. 2020).

Far-ultraviolet (FUV) photons from the star play an important role in heating disk gas and can drive massive thermal winds that eventually deplete disk material. Recent research suggests that FUV-aided dispersal and heating can have consequences for angular momentum transport through magnetocentrifugal winds (e.g., Bai et al. 2016) and the formation of planetesimals (Carrera et al. 2017). FUV photons significantly affect disk chemistry; the differences in the molecule content of low-mass TTSs and intermediate-mass Herbig stars are believed to be due to the stronger UV flux from the latter (Pascucci et al. 2014). This could have implications for the composition of planetesimals and planets that eventually form in these disks. Even after the disk is dispersed, the bright FUV flux from WTTSs could impact the evolution of (proto)planets and potentially strip their

atmospheres (Owen & Wu 2016). Characterizing FUV emission from TTSs and understanding the time evolution of the spectrum is critical to understanding disk evolution (Gorti & Hollenbach 2009) and, more fundamentally, the accretion process itself.

There have been several UV spectral surveys of TTSs by the IUE (Valenti et al. 2003) and the Space Telescope Imaging Spectrograph instruments on the Hubble Space Telescope (HST; Yang et al. 2012). While these studies have yielded valuable information on the FUV spectrum, most of the measurements of the FUV and near-ultraviolet (NUV) excesses are not simultaneous. It is thought that the NUV and the FUV flux originate from different regions of the accretion flow. The NUV Balmer continuum arises from the dense preshock region of the accretion column, and the FUV most likely arises near the hot spot (Ulrich 1976; Calvet & Gullbring 1998; Ingleby et al. 2013; Hartmann et al. 2016); this makes contemporaneous observations of both bands necessary for understanding the link between the NUV and FUV emitting regions and the nature of the accretion process (France et al. 2014; Nayak et al. 2024). UVIT on AstroSat, with its capability of accurate and simultaneous multiband UV photometry, is the ideal instrument for probing the FUV emitting regions around young stars. The use of multiple filters, three filters each in the FUV ($\lambda_{\rm eff}$ = 1481 Å, 1541 Å, and 1608 Å) and NUV ($\lambda_{\rm eff}$ = 2447 Å, 2632 Å, and 2792 Å) bands, will give us three wavelength points, allowing us to better reconstruct the flux distribution across the FUV and NUV regions.

In this paper, we present simultaneous multiband observations in the FUV and NUV bands of TTSs in the Taurus molecular cloud (TMC). We have modeled the UV flux with a blackbody spectrum and determined the corresponding temperature and luminosity. For CTTSs, the blackbody luminosity will provide a direct measure of accretion luminosity. We investigated if there is any significant difference in the blackbody temperatures between CTTSs and WTTSs, i.e., between the peak temperature for the emission due to accretion and emission due to chromospheric activity. We have also revisited the classification scheme based on the amount of UV excess emitted by TTSs over photospheric emission and the strength of the Hα emission. We also search for correlations between UV luminosity and other commonly used accretion/disk tracers such as Hα luminosity and IR excess emission.

The remaining sections of this paper are arranged as follows. In Section 2, we discuss the UVIT data, the follow-up optical spectroscopic observation from ground-based telescopes, and the SED analysis of TTSs. In Section 3, we present our results and discuss them. In the Section 4, we summarize our results from this study and their implications.

2. Data Selection and Analysis

2.1. Photometry: UVIT Observations

Four TTS fields in the TMC were observed with UVIT on board AstroSat (proposal ID: A04-210; PI: Annapurni Subramaniam). Each of these fields has a diameter of ∼28′ and was centered on the following TTSs: FM Tau, V836 Tau, BS Tau, and HD 283782. All the observations were carried out using three FUV and three NUV filters in 2018 January. The names of the FUV and NUV filters and corresponding exposure times for all targets are listed in Table 1. FM Tau is observed in the narrowband filter, N279N, centered at the Mg II line, while other TTSs are observed in the N242W wide band, keeping the other two medium bands (N245M and N263M) as common filters for all the targets.

The observations were completed in multiple orbits. We applied corrections for spacecraft drift, flat field, and distortion using the software CCDLAB (Postma & Leahy 2017) and created images for each orbit. Then, the orbit-wise images were coaligned and combined to generate final science-ready images in each filter. Astrometry was also performed using CCDLAB by comparing the Gaia DR2 source catalog. The science-ready images were created for an area of 4K × 4K in size with a scale of 0.″416 pixel^{-1}. The details about the telescope and the instruments are available in Subramaniam et al. (2016) and Tandon et al. (2017a), and the instrument calibration can be found in Tandon et al. (2017b, 2020).

We used the DAOPHOT tasks and packages in the IRAF[9] software (Stetson 1987) to carry out the photometry. To detect the sources, we used a threshold of 6 times the background variation. We performed aperture photometry on the detected stars. We applied saturation corrections to aperture magnitudes and calculated the final magnitudes of the detected stars in the AB magnitude system in the corresponding bands by adding zero-point magnitudes. The values of the zero-point magnitudes for the corresponding filters are taken from Tandon et al. (2020).

Given the large field of view (FOV) of UVIT, it is possible that other TTSs can also be present in the same FOV. To detect these serendipitous TTSs, we cataloged UVIT-detected stars in the various fields and cross-matched them with the Gaia and UV catalogs of the TMC members from Esplin & Luhman (2019), Inés Gómez de Castro et al. (2024), and Nayak et al. (2023) to search for more UV counterparts to TMC members. With UVIT, we were able to detect six more TTSs in the field of FM Tau. These are V773 Tau, CW Tau, FO Tau, CIDA 1, Anon 1, and 2MASS J04141188+2811535 (hereafter J0414). While two of the targets (V773 Tau and CW Tau) were detected in both NUV and FUV, four of the TTSs (FO Tau, CIDA 1, Anon 1, and J0414 were only detected in NUV. No additional TTSs were detected in the FOV of BS Tau, V836 Tau, and HD 283782. The final UVIT magnitudes along with the corresponding photometric errors in various filters of all 10 detected TTSs and their coordinates are listed in Table 1.

In Figure 1, we show UVIT FUV and NUV images of FM Tau and V773 Tau in different filters. DSS2 and Galaxy Evolution Explorer (GALEX) images of these three sources are also presented in the rightmost panels of Figure 1 for comparison. The images clearly show that UVIT has better resolution (∼1.″4) than GALEX. Figure 1 also shows that V773 Tau is brighter than FM Tau in the optical (DSS2); however, they appear of similar brightness in UV, and their UV magnitudes listed in Table 1 also convey the same, indicating that FM Tau exhibits strong excess emission in UV. We discuss the excess UV emissions from all the TTSs in detail in later sections.

[9] IRAF is distributed by the National Optical Astronomy Observatories, which are operated by the Association of Universities for Research in Astronomy, Inc., under a cooperative agreement with the National Science Foundation.

Table 1
The List of 10 TTS Candidates Observed with the UVIT

TTS Name (1)	R.A. (hms) (2)	Decl. (dms) (3)	Filters (NUV) (4)	Exposure Time (s) (5)	Magnitude (6)	Filters (FUV) (7)	Exposure Time (s) (8)	Magnitude (9)	Object (Type) (10)
			N245M	1221	17.46 ± 0.02	F148W	1208	19.98 ± 0.08	
FM Tau	4 14 13.6	28 12 49.2	N263M	958	16.98 ± 0.02	F154W	1207	19.75 ± 0.09	CTTS
			N279N	1211	16.56 ± 0.04	F169M	945	19.62 ± 0.11	
			N245M	1221	17.80 ± 0.03	F148W	1208	20.65 ± 0.11	
V773 Tau[a]	4 14 13.6	28 12 49.2	N263M	958	16.92 ± 0.02	F154W	1207	19.94 ± 0.10	WTTS
			N279N	1211	15.95 ± 0.03	F169M	945	20.0 ± 0.13	
			N245M	1221	16.83 ± 0.02	F148W	1208	19.38 ± 0.06	
CW Tau[a]	04 14 17.0	28 10 57.8	N263M	958	16.24 ± 0.02	F154W	1207	19.19 ± 0.07	CTTS
			N279N	1211	15.32 ± 0.02	F169M	945	18.88 ± 0.08	
			N245M	1221	19.77 ± 0.07	F148W	1208	…	
FO Tau[a]	04 14 49.3	28 12 30.46	N263M	958	19.05 ± 0.05	F154W	1207	…	CTTS
			N279N	1211	17.95 ± 0.07	F169M	945	…	
			N245M	1221	21.58 ± 0.15	F148W	1188	…	
CIDA 1[a]	04 14 17.520	28 06 9.0	N263M	958	20.61 ± 0.13	F154W	1207	…	CTTS
			N279N	1211	20.08 ± 0.17	F169M	945	…	
			N245M	1221	21.48 ± 0.15	F148W	1188	…	
J0414 +281153.3[a]	04 14 11.88	28 11 53.31	N263M	958	20.60 ± 0.13	F154W	1207	…	CTTS
			N279N	1211	19.63 ± 0.14	F169M	945	…	
			N245M	1221	21.92 ± 0.18	F148W	1188	…	
Anon 1[a]	04 13 27.216	28 16 22.8	N263M	958	20.82 ± 0.14	F154W	1207	…	WTTS
			N279N	1211	19.63 ± 0.13	F169M	945	…	
			N242W	1214	17.92 ± 0.01	F148W	1188	19.44 ± 0.06	
BS Tau	4 58 51.4	28 31 24.2	N245M	1228	18.11 ± 0.03	F154W	1190	19.24 ± 0.06	CTTS
			N263M	1225	17.83 ± 0.03	F169M	1189	19.25 ± 0.07	
			N242W	1228	19.54 ± 0.03	F148W	1199	20.68 ± 0.1	
V836 Tau	5 3 6.6	25 23 19.7	N245M	1227	19.68 ± 0.06	F154W	1200	20.32 ± 0.1	CTTS
			N263M	1205	19.05 ± 0.05	F169M	1187	20.18 ± 0.11	
			N242W	1209	16.20 ± 0.01	F148W	1193	19.08 ± 0.05	
HD 283782	4 44 54.4	27 17 45.2	N245M	1228	15.98 ± 0.01	F154W	1207	18.94 ± 0.05	WTTS
			N263M	860	15.05 ± 0.01	F169M	824	18.91 ± 0.08	

Note.
[a] In the UVIT field of FM Tau, we found six more TTS candidates having similar exposure times.

2.2. Spectroscopy: Himalayan Chandra Telescope Observation

We obtained low-resolution optical spectroscopy of all 10 TTSs. As the optical spectroscopy and UV observations are not simultaneous, it is necessary to obtain multiepoch spectra of these sources, which will allow us to identify if there is any variability in the Hα emission, i.e., variability in the accretion rate. We observed five of our targets with the Himalayan Faint Object Spectrograph Camera (HFOSC)[10] mounted on the 2 m Himalayan Chandra Telescope (HCT). We also searched the LAMOST database (Cui et al. 2012) and found optical spectra of 7 out of 10 of our targets. In Table 2, we have listed the names of the sources from which the spectra are obtained and the observation dates of different epochs for each source. We obtained multiepoch observations for all of the sources except Anon 1 and HD 283782.

For the HCT spectra, the wavelength range was covered using grism 8 (5500–9000 Å) with an effective resolving power of ∼1050. Flat frames were taken before each on-target observation, while bias frames were taken both before and after the on-target observation. The FeNe lamp spectra were also obtained after each on-target observation for wavelength calibration. The HCT spectra were reduced in a standard procedure after bias subtraction and flat-field correction using the standard tasks in the IRAF software and the HCT pipeline HAPLI (Narang et al. 2023). Then wavelength calibration was performed on the extracted spectra for further analysis.

2.3. SED

Out of 10 UVIT-detected TTS candidates, only six are detected in both the FUV and NUV bands, while the others are detected only in the NUV bands. Therefore, we performed two different approaches to fit the observed SEDs to estimate the stellar parameters. We made a two-component fit to the UV and optical part of the SEDs of the six TTSs detected in both the

[10] Further details of the instruments and telescopes are available at https://www.iiap.res.in/centers/iao/facilities/hct/hfosc/.

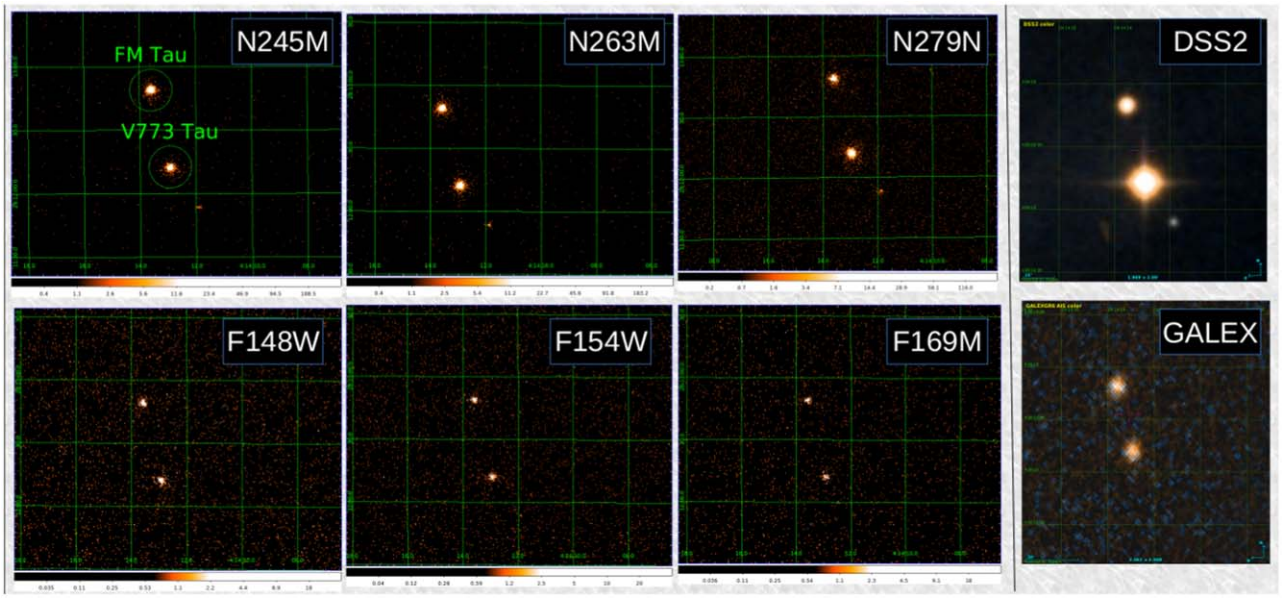

Figure 1. Multiband FUV and NUV images of FM Tau and V773 Tau are presented here. The names of the different filters are marked here. DSS2 and GALEX images are also presented for comparison.

FUV and NUV bands; we used a stellar photospheric model and a blackbody (which represents the excess over the photosphere emission due to accretion shocks) to fit the observed SEDs to determine the excess UV luminosity, its equivalent temperature, and the stellar parameters of the stars. We did not include IR regions for the SED fit, as the excess emission in the IR region comes from the disk. For the remaining four TTSs, we only fit the photospheric models of dwarf stars to the optical part of the observed SEDs to estimate stellar parameters.

To construct the observed SEDs, we cross-matched our sample with Gaia DR3 (Gaia Collaboration et al. 2021; Babusiaux et al. 2023), APASS DR9 (Henden et al. 2015), and PanSTARRS (Magnier et al. 2020) for the optical and the Two Micron All Sky Survey (2MASS; Skrutskie et al. 2006) for the IR region. We also included GALEX GR6/7 data (Bianchi et al. 2017) for this analysis. We have used the virtual observatory (VO) tool VO SED Analyzer (VOSA; Bayo et al. 2008) to generate SEDs by converting magnitudes into flux values for the corresponding filters and then to fit the observed flux distribution with theoretical model spectra. We have obtained the distances from Gaia DR3 (Bailer-Jones et al. 2021). VOSA performs multiple iterations to get the best-fit spectra to the observed flux distribution by varying $T_{\rm eff}$, $\log(g)$, metallicity, extinction, and scaling factor (M_d) values and gives the best-fit parameters after performing a χ^2 minimization. As these TTSs are in the solar neighborhood, we consider that they all have similar metallicity as the Sun. We kept extinction as a free parameter to estimate its value from the best-fit spectra. The scaling factor (M_d) is used to scale the model flux to match the observed flux and is defined as $(R_c/D)^2$, where R_c is the radius of the star and D is the distance to the star. For the stellar photosphere, we have used the BT-Settl-CIFIST model (Allard et al. 2011). We have used $\log(g)$ values between 4 and 5 and the full range for $T_{\rm eff}$ from 1200 to 7000 K. In the case of the blackbody, we used a range of temperatures from 5000 to 20,000 K.

In this study, we determined the reduced χ^2 for the best-fit SEDs, which is defined as

$$\chi^2_{\rm reduced} = \frac{1}{N-n}\sum_{k=1}^{N}\frac{(F_{o,k} - M_d \times F_{m,k})^2}{{\sigma_{o,k}}^2}\,, \qquad (1)$$

where N is the number of photometric data points, n is the number of input-free parameters, $F_{o,k}$ is the observed flux, and $F_{m,k}$ is the model flux. Though χ^2 is used to determine the quality of the fit, χ^2 values are often found to be larger despite visual inspection suggesting them to be well-fitted SEDs. This large χ^2 value arises when the photometric data points have very small observational flux errors (say, <1% of the observed flux). So, even if the model reproduces the observation apparently well, the deviation can be much higher than the reported observational error (increasing the value of χ^2; Rebassa-Mansergas et al. 2021). To mitigate this, VOSA has introduced the parameter called the visual goodness of fit (Vgf_b) by modifying the χ^2 formula, where the error is considered to be at least 10% of its observed flux.[11] The parameter Vgf_b provided by VOSA with a value of $\leqslant$15 is usually considered as a proxy for well-fitted SEDs (Rebassa-Mansergas et al. 2021). We considered the Vgf_b parameter for the goodness of fit; however, we mentioned both the χ^2 and Vgf_b parameters from the SED fitting process.

In Figure 2, we have shown the SEDs of the six TTSs (detected in both the FUV and NUV) fitted with model spectra. The observed fluxes are shown as cyan and blue points, where cyan points fall in the UV and optical regions of the energy distribution, which is included in the dual-component fitting of model spectra. The blue points fall in the IR region and are not included in the fit. The black and gray lines represent the best-fit blackbody and BT-Settl-CIFIST spectra, respectively, to the cyan points. The combined flux of these two model spectra is shown as the red line. The red points indicate the combined

[11] http://svo2.cab.inta-csic.es/theory/vosa/helpw4.php?otype=star&action=help

Table 2
Spectroscopic Observations

Source	Instruments	Observation Date (yyyy-mm-dd)	EW(Hα)	$\overline{\mathrm{EW(H\alpha)}}\|^{\mathrm{min}}_{\mathrm{max}}$	L_{acc} $L_{\odot}$	$\dot{M}_{\mathrm{acc}}$ ($\times 10^{-9}$ $M_{\odot}$ yr^{-1})	Classification
(1)	(2)	(3)	(4)	(5)	(6)	(7)	(8)
Anon 1	LAMOST	2014-11-05	-3.9 ± 0.2	-3.9	⋯	⋯	WTTS
BS Tau	HCT	2021-01-17	-31.1 ± 1.2	-33.1 ± 2.0	0.011 ± 0.001	$2.17^{-0.16}_{+0.16}$	CTTS
		2021-09-06	-35.1 ± 1.3	⋯	⋯	⋯	⋯
CIDA 1	LAMOST	2012-01-04	-141.9 ± 34.3	$-205.5^{+107.8}_{-67.7}$	$0.004^{-0.002}_{+0.001}$	$0.70^{-0.41}_{+0.28}$	CTTS
		2011-12-18	-224.8 ± 21.6	⋯	⋯	⋯	⋯
		2012-01-13	-133.3 ± 16.4	⋯	⋯	⋯	⋯
		2012-01-22	-97.7 ± 7.3	⋯	⋯	⋯	⋯
		2013-02-08	-271.7 ± 18.9	⋯	⋯	⋯	⋯
		2014-01-25	-242.1 ± 28.2	⋯	⋯	⋯	⋯
		2015-10-13	-231.5 ± 26.7	⋯	⋯	⋯	⋯
		2015-12-28	-273.2 ± 47.6	⋯	⋯	⋯	⋯
		2016-12-31	-232.9 ± 11.9	⋯	⋯	⋯	⋯
CW Tau	LAMOST	2014-01-25	-87.1 ± 2.3	$-126.8^{+39.7}_{-105.4}$	$0.54^{-0.195}_{+0.57}$	$107.69^{-38.8}_{+113.65}$	CTTS
		2014-01-30	-232.2 ± 7.2	⋯	⋯	⋯	⋯
		2014-11-05	-60.4 ± 1.8	⋯	⋯	⋯	⋯
FM Tau	LAMOST	2014-01-30	-112.8 ± 3.6	$-118.8^{+18.1}_{-24.1}$	$0.083^{-0.015}_{+0.021}$	$16.75^{-2.99}_{+4.12}$	
	HCT	2021-01-17	-100.7 ± 3.7	⋯	⋯	⋯	⋯
		2021-09-06	-142.9 ± 4.2	⋯	⋯	⋯	⋯
FO Tau	LAMOST	2011-12-18	-136.4 ± 9.3	$-143.5^{+8.3}_{-29.2}$	$0.059^{-0.004}_{+0.014}$	$11.68^{-0.80}_{+2.88}$	CTTS
		2012-01-04	-172.7 ± 13.4	⋯	⋯	⋯	⋯
		2012-01-13	-135.9 ± 9.4	⋯	⋯	⋯	⋯
		2013-02-08	-135.2 ± 9.3	⋯	⋯	⋯	⋯
		2014-01-25	-137.4 ± 7.5	⋯	⋯	⋯	⋯
		2014-01-30	-158.2 ± 11.2	⋯	⋯	⋯	⋯
HD 283782	HCT	2021-09-06	-1.9 ± 0.1	-1.9	⋯	⋯	WTTS
V773 Tau	LAMOST	2014-11-05	-3.2 ± 0.1	$-2.5^{+0.6}_{-0.7}$	⋯	⋯	WTTS
	HCT	2021-09-06	-1.9 ± 0.1		⋯	⋯	⋯
V836 Tau	HCT	2021-01-17	-8.9 ± 0.5	$-13.3^{+4.4}_{-4.3}$	$0.013^{-0.005}_{+0.005}$	$2.60^{-1.0}_{+1.0}$	CTTS
		2021-09-06	-17.6 ± 0.5	⋯	⋯	⋯	⋯
J0414	LAMOST	2012-01-22	-319.4 ± 35.6	$-357.4^{+38.0}_{-47.2}$	$0.002^{-0.001}_{+0.001}$	$0.49^{-0.01}_{+0.01}$	CTTS
		2012-01-23	-404.6 ± 138.3	⋯	⋯	⋯	⋯
		2015-12-28	-348.2 ± 69.7	⋯	⋯	⋯	⋯

Note. Column (5) represents the average value of EW(Hα) from multiepoch observations as listed in column (4), and the uncertainties denote the range of EW(Hα) from multiepoch observations. The uncertainties in L_{acc} and $\dot{M}_{\mathrm{acc}}$ listed in columns (6) and (7), respectively, represent the range in these values due to the range in EW(Hα) values.

flux in different bands. The overlap between the red and cyan points indicates the goodness of the two-component fitting. We notice that in the case of HD 283782, the combined flux matches very well in the IR region (not included in the fit) as well. Therefore, there is no IR excess present in HD 283782, which indicates that the TTS does not have hot/warm dust around it. The values of reduced χ^2, Vgf_b, temperature, log$g$, and extinction (A_V) corresponding to the best-fit spectra are noted in the legends. The names of the sources are mentioned at the top of each plot. V836 Tau and HD 283782 are found to have high χ^2 values (>100) due to the abovementioned reason of very small photometric error; however, smaller values of Vgf_b (<5) indicate that SEDs are fitted well by the model spectra.

In Figure 3, we have shown SEDs of TTSs with no FUV detections. Due to the absence of FUV points, only the optical region of the observed SED is fitted with synthetic dwarf spectra (BT-Settl-CIFIST) to get the stellar parameters of these TTSs. Fitting two-component spectra to these sources with no FUV data points leads to the wrong estimation of parameters for the blackbody and stellar spectrum. We arrived at this conclusion after examining two-component fits to those six TTSs having both FUV and NUV, but FUV data points were not included in the fitting process, and found that the best-fit spectra were not able to produce the observed FUV flux. We have used T_{eff}, log (g), and A_V as free parameters and metallicity to be fixed at the solar value. Blue and cyan points in Figure 3 are observed SEDs, where only the cyan points are included in the fitting process. The gray spectrum indicates the best-fit model spectrum to the optical region of the observed SED. The red points indicate the expected flux due to the best-fit model spectrum. The best-fit parameters are mentioned in the legend. Except for the source J0414, all the other sources have very high χ^2 values; however,

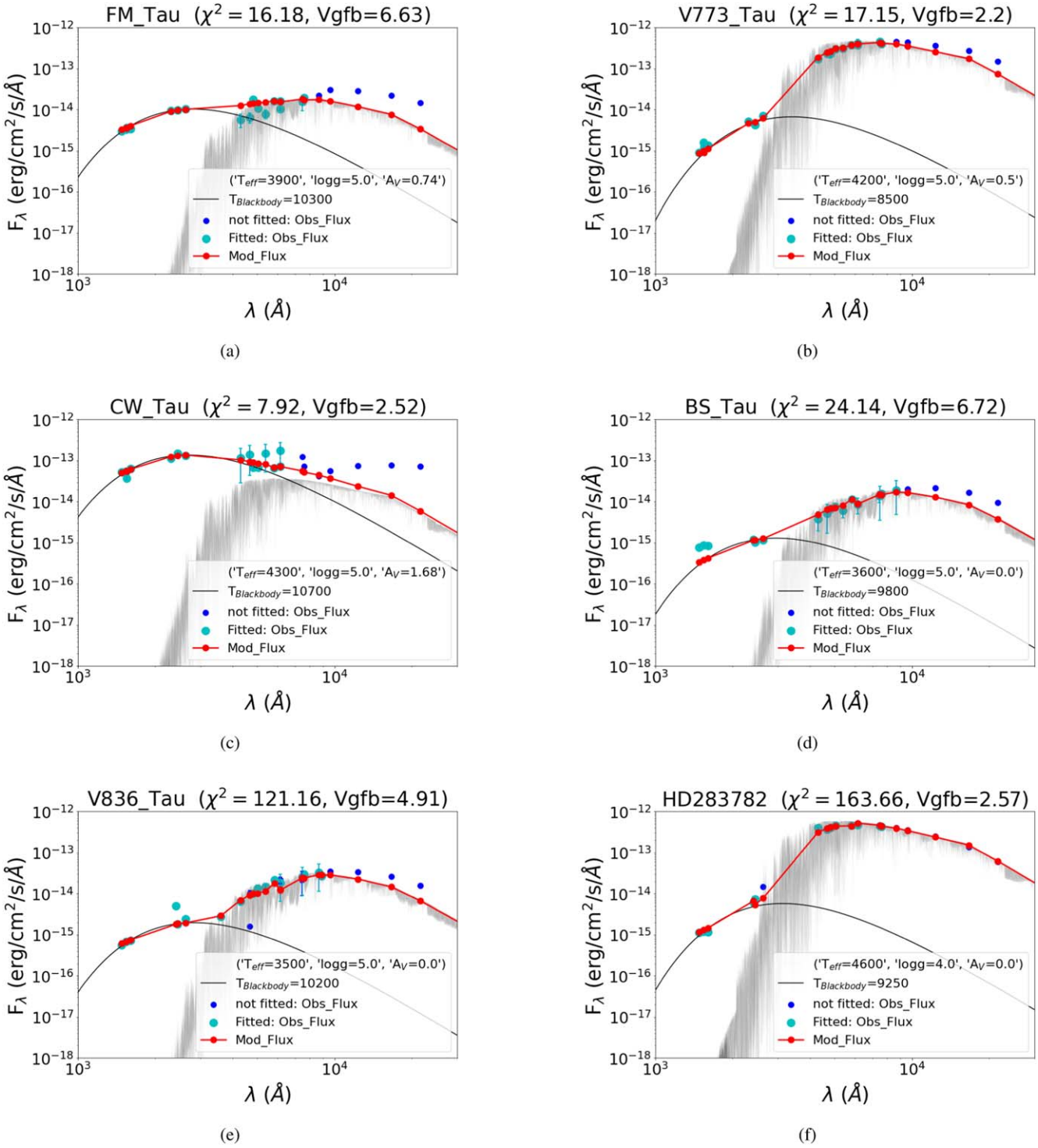

Figure 2. SEDs of TTSs are shown here. The names of the TTSs and the best-fit values of χ^2 and Vgf_b are mentioned on top of each subfigure. The gray and black lines represent the best-fit synthetic blackbody and dwarf spectra, respectively, on the observed fluxes (cyan and blue points). Cyan points are included in the fitting algorithm, avoiding the NIR region, marked as blue. The red line indicates the expected combined model flux from the fitted synthetic spectra. The best-fit parameters for dwarf and blackbody spectra are also mentioned in the legend of each subfigure.

all four sources have $Vgf_b \leqslant 15$, suggesting that the model spectra fitted well to the observed SEDs.

3. Results and Discussion

The SED analysis provides us with the fundamental parameters of the TTSs, i.e., $T_{\rm eff}$, log(g), radius, mass, and bolometric luminosity ($L_{\rm bol}$) of the central stars. As mentioned on the VOSA website, the fitting process and the predicted flux are relatively less sensitive to $\log g$. This poses a challenge to put direct constraints on the masses of the components, since a slight change in $\log g$ can create a large difference in the estimated mass. Therefore, we do not include the estimations of mass and $\log g$ in our analysis. The values of the other

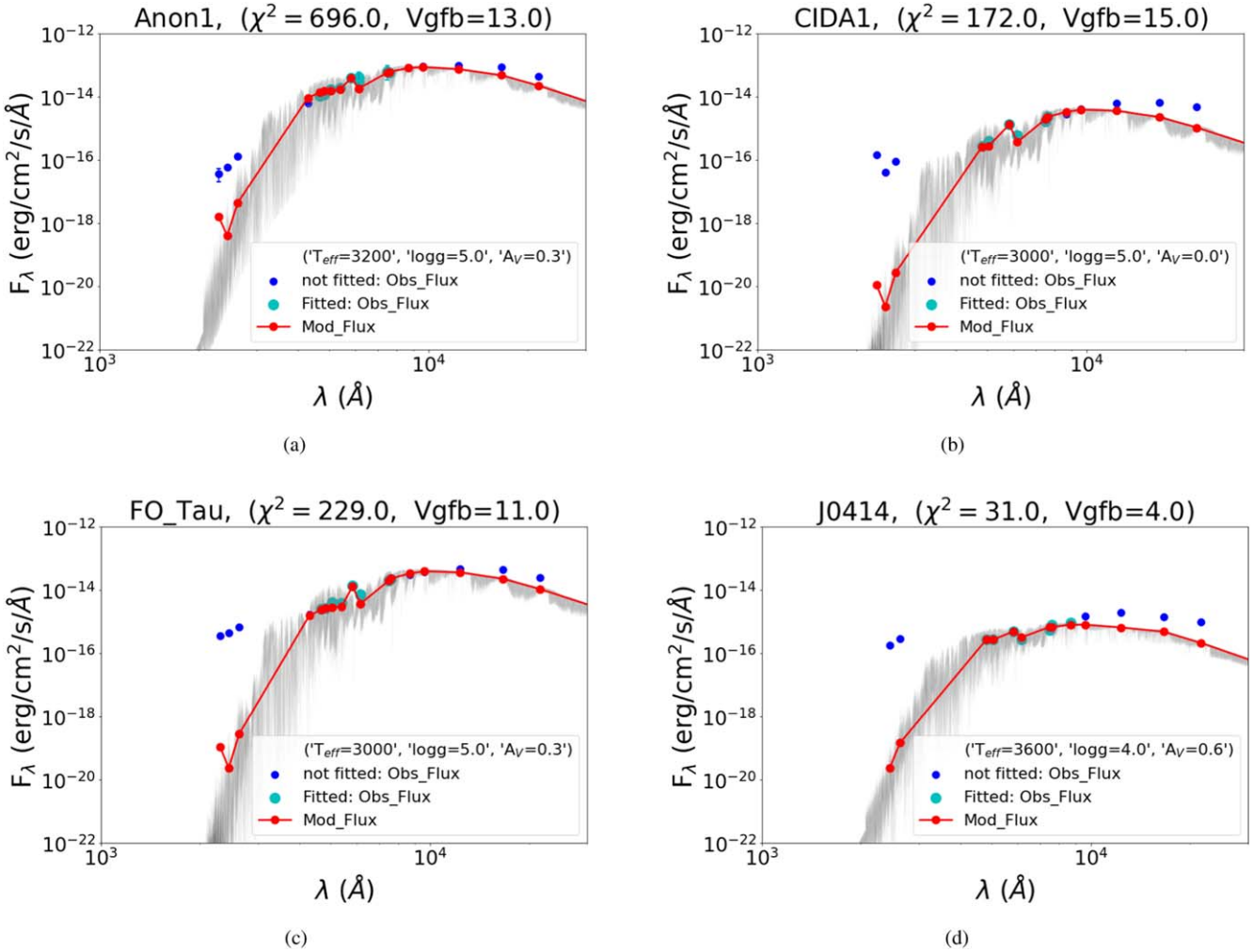

Figure 3. The figure is the same as Figure 2, but only the optical regions of the SEDs are fitted with theoretical dwarf spectra (BT-Settl-CIFIST), avoiding the UV and NIR regions.

Table 3
Stellar Properties Estimated from SED Analysis

TTS Name (1)	T_{BB} (K) (2)	T_{eff} (K) (3)	Radius ($R_\odot$) (4)	L_{bol} ($L_\odot$) (5)	Spectral Type (6)	L_{acc} ($L_\odot$) (7)	$\dot{M}_{acc}$ ($10^{-9} \times M_\odot$ yr^{-1}) (8)
FM Tau	10,300	3900	0.73 ± 0.03	0.11 ± 0.001	K7	0.022 ± 0.0002	4.44 ± 0.03
V773 Tau	8500	4200	3.02 ± 0.03	2.54 ± 0.02	K6	0.018 ± 0.0002	⋯
BS Tau	9800	3600	0.96 ± 0.03	0.14 ± 0.003	M2	0.004 ± 0.0001	0.78 ± 0.03
V836 Tau	10,200	3500	1.54 ± 0.04	0.33 ± 0.003	M3	0.01 ± 0.0001	1.93 ± 0.03
HD 283782	9250	4600	3.34 ± 0.05	4.45 ± 0.028	K4	0.073 ± 0.0006	⋯
CW Tau	10,700	4300	0.81 ± 0.03	0.21 ± 0.002	K5.25	0.325 ± 0.004	64.9 ± 0.09
FO Tau	⋯	3000	2.24 ± 0.07	0.37 ± 0.001	M6.5	⋯	⋯
Anon 1	⋯	3200	2.59 ± 0.04	0.64 ± 0.001	M5	⋯	⋯
J0414	⋯	3600	0.20 ± 0.04	0.006 ± 0.001	M2	⋯	⋯
CIDA 1	⋯	3000	0.61 ± 0.04	0.027 ± 0.001	M6.5	⋯	⋯

parameters are listed in Table 3. The luminosity of the blackbody provides a direct measure of the accretion luminosity/chromospheric luminosity. In Table 3, we list the value of bolometric luminosity enclosed within the blackbody spectrum (L_{acc}) and blackbody temperature (T_{BB}). We have also estimated the spectral type of each TTS using the T_{eff}–spectral type relation (Pecaut & Mamajek 2013), listed in column (6) of Table 3. We find that TTSs have a T_{eff} range from 3000 to 4600 K and spectral types of K and M. The T_{BB} ranges from 8500 to 10,700 K.

3.1. UV Excess as an Indicator of Accretion

We notice in Figure 2 that V773 Tau and HD 283782 emit negligible amounts of excess emission in the NUV bands above the photospheric emission compared to that found in the FUV

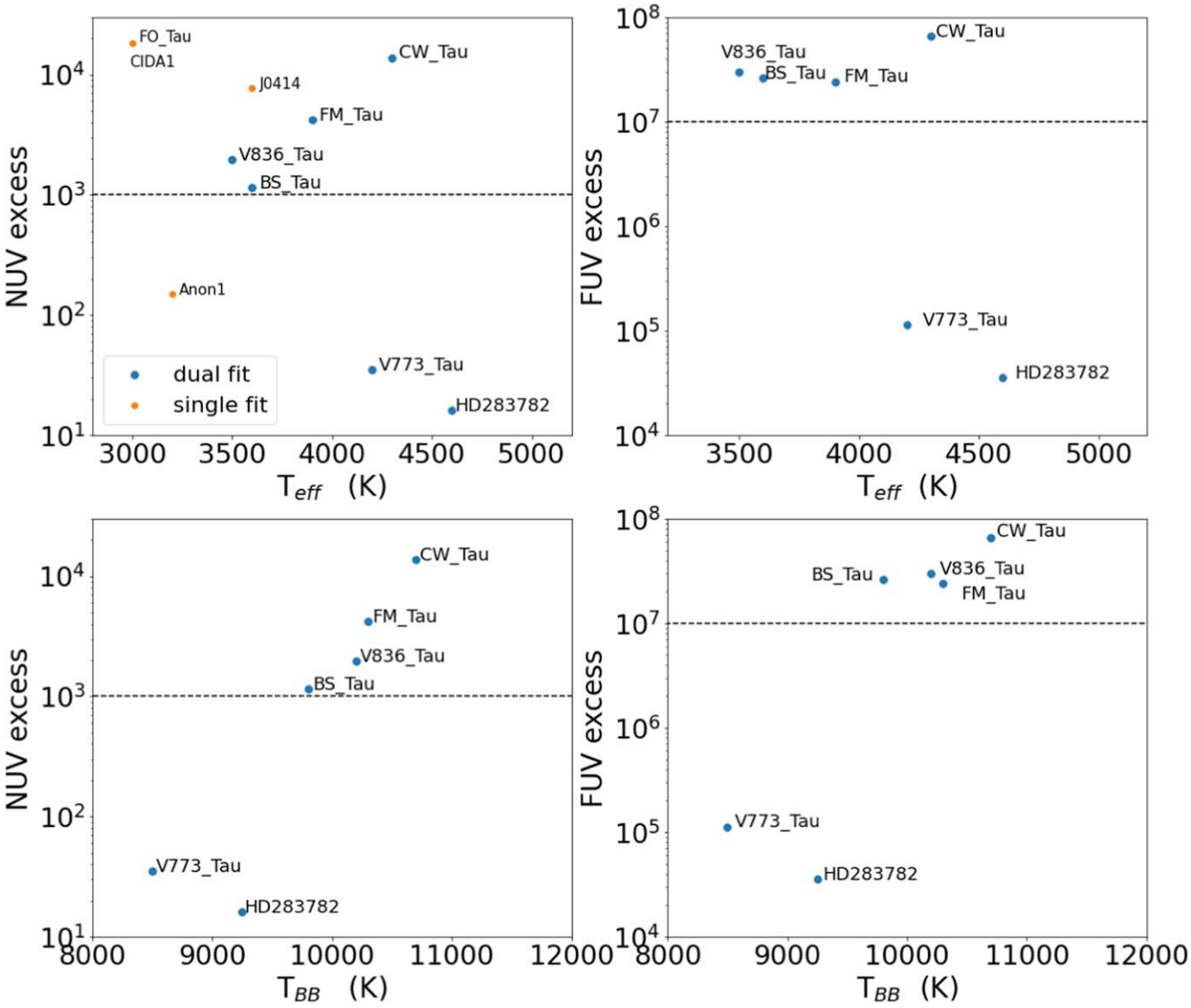

Figure 4. The relations of UV excess as a function of effective temperature ($T_{\rm eff}$; top panels) and blackbody temperature ($T_{\rm BB}$; bottom panels) are shown here. The horizontal dashed line shows the nominal separation between stars with active accretion and chromospheric activity.

bands. However, in the other four sources, we observe a large excess emission in both the NUV and FUV bands. In Figure 3, we further notice that Anon 1 has fewer excess NUV bands compared to other sources. The presence/absence of NUV excess appears to divide sources into two different categories.

However, we need to quantitatively estimate the amount of excess emission in all the sources and compare them before giving any conclusion. To quantify the excess flux observed in the FUV and NUV regions, we define excess emission in a particular band as $\left(\frac{(\text{dereddened observed flux})}{(\text{model flux})_{\rm BT-Settl-CIFIST}} - 1\right)$. To demonstrate UV excess, we used the N245M filter in the NUV and the F148W band in the FUV regions, as these are common bands for all the sources. We have plotted the NUV and FUV excess as a function of effective temperature ($T_{\rm eff}$) in the upper panels of Figure 4 and as a function of blackbody temperature ($T_{\rm BB}$) in the lower panels. $T_{\rm eff}$ and $T_{\rm BB}$ are estimated from SED fitting. The sources detected in both FUV and NUV are marked as blue points, while the sources with only NUV detections are marked in orange. We can see that there are two groups, independent of their spectral types and blackbody temperature, separated by a black dashed line. The presence of a high UV excess ($>10^3$ in NUV and $>10^7$ in FUV) suggests that these seven sources (FM Tau, CW Tau, BS Tau, V836 Tau, CIDA 1, FO Tau, and J0414) could be still actively accreting, while V773 Tau, HD 283782, and Anon 1 are probable nonaccreting WTTS candidates with comparatively little excess in UV. Comparatively low UV excess with almost no IR excess in HD 283782 indicates that it is an example of a diskless WTTS. A more careful inspection suggests that stars with higher UV excess (or the probable CTTSs) also tend to have hotter $T_{\rm BB}$ compared to the stars with lesser UV excess. However, we need more sources with simultaneous UV observations to confirm this aspect. We classify the stars emitting $>10^3$ ($>10^7$) excess emission in NUV (FUV) as CTTSs, while the other group of stars is classified as WTTS. Our classification based on the UV excess is listed in Table 1. However, a strong UV flare might also cause excess UV emission and appear as CTTSs in Figure 4. Therefore, we require further evidence from spectroscopic observations before confirming their classification as CTTSs or WTTSs, as CTTSs are expected to show strong Hα emission compared to WTTSs.

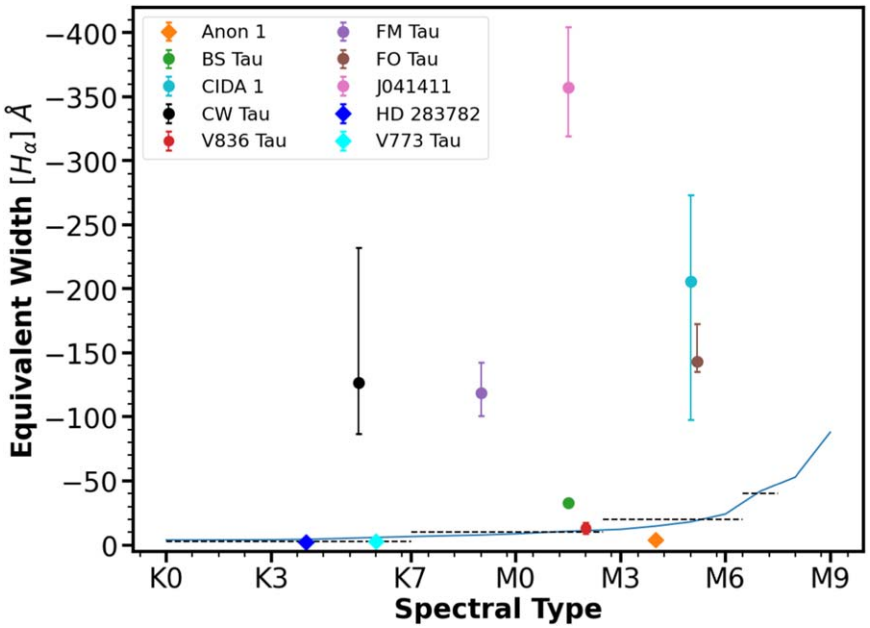

Figure 5. The mean Hα EWs ($\overline{\mathrm{EW(H\alpha)}}|^{\mathrm{min}}_{\mathrm{max}}$) from multiepoch observations of TTSs are plotted as a function of their spectral types. The vertical lines represent the range of EW(Hα) from multiepoch observations, as listed in Table 2. A little offset is applied to FO Tau along the spectral types to avoid its overlap with CIDA 1. The solid line (Barrado y Navascués & Martín 2003) and dashed line (White & Basri 2003) indicate relations between spectral types and EW(Hα), which separates CTTSs (circles) from WTTSs (diamonds).

3.2. Hα Line Emission as an Accretion Indicator

We analyzed spectra obtained from both the HFOSC/HCT and LAMOST for our sources. We estimated the equivalent width of Hα line emission (EW(Hα)) after subtracting continuum flux from the spectra. In Table 2, we have listed the EW(Hα) along with its measurement error for each source obtained from the multiepoch observations with different telescopes (column (4)). The names of the telescopes and the dates of the observations are also mentioned in columns (2) and (3), respectively. We notice that the EW(Hα) of FM Tau and V773 Tau from HCT observations matches well with that obtained from the LAMOST spectra. We are unable to obtain a multiepoch of observation for Anon 1 and HD 283782. In column (5), we have listed average values of EW(Hα) corresponding to each TTS, and the errors associated with it indicate the range in EW(Hα) from multiepoch observations ($\overline{\mathrm{EW(H\alpha)}}|^{\mathrm{min}}_{\mathrm{max}}$). All the sources except J0414 are found to have smaller measurement uncertainties in EW(Hα) compared to its range from multiepoch observations. As the strength of Hα provides an indirect indication of accretion rate, a large range in EW(Hα) with relatively smaller observational errors in CIDA 1 and CW Tau suggests a large variation in accretion rate in these TTSs.

The Hα line strength has often been used to distinguish between CTTSs and WTTSs in the literature (White & Basri 2003). WTTSs show weak emission due to chromospheric activity, while comparatively strong emission from CTTSs is produced due to accretion. However, there is no unique value of EW(Hα) that acts as a dividing line for this classification (Barrado y Navascués & Martín 2003; White & Basri 2003). Barrado y Navascués & Martín (2003) provided EW(Hα) values as a function of spectral types, derived from the observed saturation limit for the chromospheric activity (blue line in Figure 5), whereas White & Basri (2003) provided maximum EW(Hα) values for WTTSs for different ranges in spectral types (black dashed line in Figure 5). We have overplotted $\overline{\mathrm{EW(H\alpha)}}|^{\mathrm{min}}_{\mathrm{max}}$ values of our sample TTSs in Figure 5. The spectral types are estimated from the photospheric temperature based on the correlation given in Pecaut & Mamajek (2013), listed in Table 3. Figure 5 shows that FM Tau, BS Tau, CW Tau, CIDA 1, FO Tau, and J0414 have high values of EW(Hα) with respect to the expected values from WTTSs with similar spectral types. These stars also show high UV excess, as discussed in the previous section, indicating that their classification as CTTSs is robust. Except for BS Tau, all other sources discussed above show significant variation in the EW(Hα), suggesting a large variation in the accretion rate. J0414 has a large uncertainty in the estimation of EW(Hα), so variation in J0414 is most likely not due to accretion variability. In the next section, we estimate and discuss the accretion luminosity and mass accretion rate of these sources. However, we need more follow-up observations for a detailed study of their variability.

Anon 1, V773 Tau, and HD 283782 have EWs less than that expected for their spectral types, which indicates that these TTSs can be classified as WTTSs, marked as diamonds in Figure 5. From the SEDs, we have also seen a relatively low UV excess over photospheric emission. Both these scenarios suggest that these are WTTSs. Figure 5 also shows that V836 Tau falls on the line separating CTTSs from WTTSs and the range in the EW(Hα) extends on both sides, making it difficult to classify. However, we notice a large amount of UV excess emission as shown in Figure 4, which is comparable to that found in other CTTSs, suggesting that V836 Tau is a CTTS. We also notice that V836 Tau changes its EW from 8.88 to 17.6 in the two epochs of observation, which corresponds to a $\sim$100% increase in the EW. These observations suggest that the star is going through a variable accretion rate. Therefore, based on both UV excess and EW(Hα), we suggest that V836 Tau is a slowly accreting CTTS with a variable accretion rate. Further monitoring observations of V836 Tau are required to

understand its accretion properties. Our classification based on the spectroscopic observations is listed in Table 2.

Our classification of these sources matches well with the previous literature. From the literature, we find that FM Tau, CW Tau, and FO Tau are classified as CTTSs, while V773 Tau and HD 283782 are classified as WTTSs (Herbig & Bell 1988; Kenyon et al. 1998; Valenti et al. 2003; Ingleby et al. 2013; McClure et al. 2013; Gómez de Castro et al. 2015), which agrees with our classification. BS Tau and V836 Tau are classified as WTTSs based on the UV–NIR color–color relation (Gómez de Castro et al. 2015), contrary to our classification of CTTSs for both sources. Based on HST FUV spectroscopic observations, V836 Tau is classified as a slowly accreting CTTS (Ingleby et al. 2013). However, both UV excess and EW(Hα) values from our analysis indicate that BS Tau and V836 Tau are CTTSs. We did not find any classification for CIDA 1, J0414, and Anon 1 in the literature. Thus, from our analysis, we reconfirm that V836 Tau is a CTTS, and for the first time, we report that BS Tau, CIDA 1, and J0414 are CTTSs and Anon 1 is a WTTS. This study demonstrates the importance of multiwavelength SED analysis and, in particular, simultaneous FUV and NUV observations to classify the TTSs as CTTSs or WTTSs.

3.3. Relation between Hα Luminosity and Accretion Luminosity

In this study, we have determined the excess UV flux by fitting the excess emission with the blackbody spectrum. The flux enclosed within the fitted blackbody spectrum is nothing but the excess UV emission due to accretion in CTTSs and chromospheric activity in the WTTSs. Hence, the bolometric luminosity of the blackbody spectrum provides a direct measure of accretion luminosity in CTTSs. We used this luminosity value to calculate the mass accretion rate in CTTSs. Mass accretion rate ($\dot{M}$) and accretion luminosity are related by the following equation by Gullbring et al. (1998):

$$L_{\rm acc}/L_{\odot} = (GM_{*}\dot{M}/R_{*}) \times (1 - R_{*}/R_{\rm in}), \quad (2)$$

where M_{*} and R_{*} are the stellar mass and radius and $R_{\rm in}$ is the disk truncation radius from which the gas falls onto the star. $R_{\rm in}$ is typically assumed to be $\sim 5\,R_{*}$ (Gullbring et al. 1998). The error introduced by this assumption on the measured mass accretion rates, considering that $R_{\rm in}$ for a pre-main-sequence star can span from 3 to $8\,R_{*}$, is less than 20%. Therefore, the above equation can be written as

$$\dot{M}_{\rm acc} = (1 - R_{*}/R_{\rm in}) \times (L_{\rm acc}R_{*}/GM_{*}) \sim 1.25(L_{\rm acc}R_{*}/GM_{*}). \quad (3)$$

We have considered $R_{*}/M_{*} \sim 5\,R_{\odot}/M_{\odot}$ and used Equation (3) to estimate $\dot{M}_{\rm acc}$. The values are listed in the last column of Table 3. We have only calculated the mass accretion rate for the stars classified as CTTSs. $L_{\rm acc}$ and $\dot{M}_{\rm acc}$ as estimated from excess UV flux provide a direct measure of these parameters.

EW(Hα) is often used as a proxy for accretion (White & Basri 2003). However, EW(Hα) is a secondary indicator for accretion. Therefore, we tried to find the correlation between $L_{\rm acc}$ from UV excess and $L_{\rm H\alpha}$. We used extinction-corrected PanSTARRS r-band flux density as a proxy for the continuum flux density underlying the Hα line and the distance obtained from Gaia DR3 to calculate $L_{\rm H\alpha}$ from the average EW(Hα) values listed in Table 2. The continuum flux density at Hα is given as (Mathew et al. 2018)

$$F_{\nu,\rm cont}(\rm H\alpha) = F_{\nu,0} \times 10^{\left(\frac{-r_0}{2.5}\right)},$$

where $F_{\nu,0} = 3.08 \times 10^{-23}\,\rm W\,m^{-2}\,Hz^{-1}$ and r_0 is the extinction-corrected PanSTARRS magnitude. The extinction is obtained from the SED fitting as listed in Table 3. In Figure 6, we plotted $L_{\rm acc}$ estimated from UV excess versus that estimated from ($L_{\rm H\alpha}$), which shows a linear correlation (red line) between them with a slope of 1.20 ± 0.22 and intercept of 2.16 ± 0.70. The uncertainties associated with $L_{\rm H\alpha}$ shown in Figure 6 mainly signifies the range in $L_{\rm H\alpha}$ values from $\overline{\rm EW(H\alpha)}|^{\rm min}_{\rm max}$. The uncertainties in $L_{\rm acc}$ or UV luminosities are obtained from the observational errors in flux and distance estimations, not from the errors in the best-fit model parameters. As both observed flux errors and distance errors are very small, the uncertainties in $L_{\rm acc}$ are also found to be very small. There are also previously reported correlations between $L_{\rm H\alpha}$ and $L_{\rm acc}$ (Vogt et al. 1994; Dahm 2008; Herczeg & Hillenbrand 2008; Fang et al. 2009; Ingleby et al. 2013). We compare our relation with that estimated by previous studies in Table 4 and notice that our relation matches quite well with the slope and intercept values with the previous estimation from the literature. However, we get a relatively large error in its intercept value, which could be due to the small sample size and nonsimultaneous observation of Hα and UV. A large sample with simultaneous observations in UV and optical spectroscopy is required for a better correlation. We have also used this relation to estimate $L_{\rm acc}$ from $L_{\rm H\alpha}$ for all the CTTSs listed. This helps us to calculate $L_{\rm acc}$ for the TTSs with no FUV observations for which we could not estimate UV luminosity. We then also calculated $\dot{M}_{\rm acc}$ using Equation (3). The values of $L_{\rm acc}$ and $\dot{M}_{\rm acc}$ are listed in columns (6) and (7) of Table 2, respectively. The uncertainties associated with $L_{\rm acc}$ and $\dot{M}_{\rm acc}$ indicate the range in these values due to the range in $\overline{\rm EW(H\alpha)}|^{\rm min}_{\rm max}$. We notice that J0414, CIDA 1, V836 Tau, and

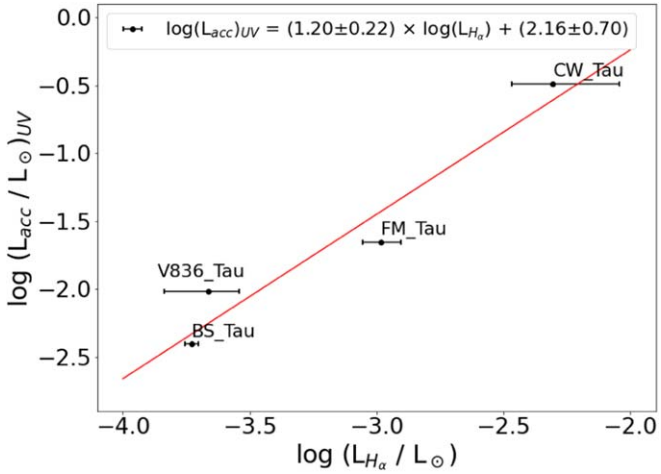

Figure 6. The figure shows the relation between accretion luminosity estimated using UV luminosity and Hα luminosity ($L_{\rm H\alpha}$). The uncertainties in $L_{\rm H\alpha}$ are calculated from the range in EW(Hα), obtained from multiepoch spectroscopic observations. The red line represents the linear fit to the data points, and the linear relation is noted in the legend. The relatively large residuals are expected since the Hα and UV data were not taken simultaneously.

Table 4
Comparing the Empirical Relation between L_{acc} and $L_{H\alpha}$ Found in Figure 6 with Literature Values

Slope (m)	Intercept (c)	Reference
1.20 ± 0.11	2.0 ± 0.4	Herczeg & Hillenbrand (2008)
1.18 ± 0.26	2.19 ± 0.64	Dahm (2008)
1.25 ± 0.07	2.27 ± 0.23	Fang et al. (2009)
1.31 ± 0.03	2.63 ± 0.13	Manara et al. (2012)
1.0 ± 0.2	1.3 ± 0.7	Ingleby et al. (2013)
1.20 ± 0.22	2.16 ± 0.70	This work

Note. The formulation used is $\log(L_{acc}/L_{\odot}) = m \times \log(L_{H\alpha}/L_{\odot}) + c$.

BS Tau are the slowly accreting CTTSs with a mass accretion rate of a few times $10^{-9}\,M_{\odot}\,yr^{-1}$, while FM Tau, CW Tau, and FO Tau are found to have a comparatively higher accretion rate (a few times $10^{-8}\,M_{\odot}\,yr^{-1}$).

3.4. Relation between UV Excess and IR Excess

The NIR color excess is taken as evidence for the presence of circumstellar disks around TTSs. The strength of the infrared color excess indicates the amount of dust and gas in these disks. A strong excess suggests a substantial amount of material in the disk, while a weaker excess may indicate a less massive or more evolved disk. The strong excess in FUV and NUV suggests the presence of significant accretion onto the stars. In contrast, the high FUV and relatively low or no NUV excess suggest that the UV emission originates from chromospheric activity. FUV emission from the star plays a significant role in heating gas disks and driving massive thermal winds that deplete the disk material. Hence, an excess in (FUV–NUV) color in WTTSs will tell us if the stars are dominant in chromospheric activity, while for CTTSs, it tells us whether the stars are dominant in FUV emission. Also, the comparison between UV color and IR color helps us to identify the changes in disk morphology (primordial gas-rich disks or evolved or transitioning to a debris disk) from FUV-bright stars to FUV-faint stars. The UV color index is plotted against $J-K$ infrared color excess from 2MASS observations in Figure 7. $J-K$ excess is considered to be a good estimator of the accretion rate (Meyer et al. 1997). The color excess is defined as $-2.5 \times \left[\log\left(\frac{(\text{observed flux})_{\text{Band1}}}{(\text{observed flux})_{\text{Band2}}}\right) - \log\left(\frac{(\text{expected flux})_{\text{Band1}}}{(\text{expected flux})_{\text{Band2}}}\right)\right]$ in magnitude units. For CTTSs, we notice that stars with a lower IR color excess, i.e., with weaker inner disks, appear bluer in the (FUV–NUV) color, which means they have stronger FUV emission. This suggests that strong FUV emission might have caused the depletion of the gas and dust in the circumstellar disk in CTTSs. The WTTSs seem to be following a different slope relation compared to CTTSs, but with two WTTS data points, it is not so conclusive. A larger sample of CTTSs and WTTSs is required for a better understanding of this relation.

4. Summary

In this study, we present the accretion properties of 10 TTSs in the TMC, namely, FM Tau, BS Tau, V836 Tau, HD 283782, V773 Tau, CW Tau, FO Tau, Anon 1, CIDA 1, and J0414. This is the first UVIT study of TTSs and highlights the significance of simultaneous multiband UV observations of TTSs to study their accretion properties. Six of the 10 are detected in both the FUV and NUV bands, while the remaining four are detected only in the NUV. We report, for the first time, the UV photometry of J0414 (not detected in GALEX, which could be due to a short exposure time).

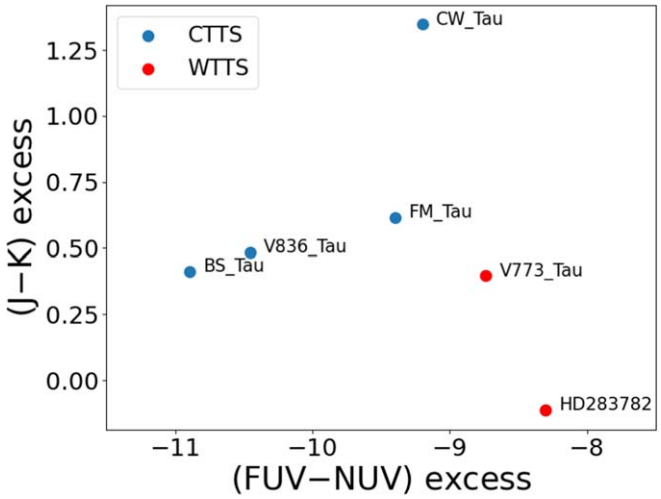

Figure 7. The figure shows the relation between IR excess and UV excess.

For the sources detected in both FUV and NUV, we modeled the excess UV flux emitted by TTSs as blackbody emission and measured the excess UV emission by two-component SED fitting to the UV and optical regions of the observed SED. From the SED fit, we obtained the fundamental stellar parameters (temperature, extinction, radius, and bolometric luminosity) of these TTSs. We also estimated the blackbody temperature and luminosity corresponding to the excess UV emission. For the sources with only NUV detection, we only fit the optical region of the SEDs to obtain the stellar parameters and excess emission in the NUV bands.

We noticed there are two categories of TTSs based on the excess UV emission: one shows strong excess emission ($>10^3$ in NUV and $>10^7$ in FUV) over the photosphere, and the other has excess emission mostly in FUV ($\lesssim 10^5$) and a little excess in NUV ($\lesssim 10^2$). We classify the TTSs with strong excess emission in both FUV and NUV as CTTSs and the other group as WTTSs. This study shows that UV excess can be used as a tool to distinguish CTTSs and WTTSs.

We found that the classification of TTSs as CTTSs or WTTSs based on the spectral type versus EW(Hα) relation (Barrado y Navascués & Martín 2003; White & Basri 2003) matches well with that made based on UV excess. Our classification also matches well with the literature. From our analysis, we reconfirm that V836 Tau is a CTTS. For the first time, we report that BS Tau, CIDA 1, and J0414 are still actively accreting and classify them as CTTSs, and we classify Anon 1 as a nonaccreting or WTTS.

We found that Hα luminosity and accretion luminosity (from UV luminosity) are linearly correlated with a slope of 1.20 ± 0.22 and an intercept of 2.16 ± 0.70. The correlation also matches well with previous estimates by Dahm (2008), Herczeg & Hillenbrand (2008), Fang et al. (2009), and Manara et al. (2012). From the mass accretion rate calculation based on UV luminosity and Hα luminosity, we found that CW Tau, FM Tau, and FO Tau are going through a strong accretion phase with an accretion rate $>10^{-8}\,M_{\odot}\,yr^{-1}$, while other CTTSs are accreting at a slower rate (~a few times $10^{-9}\,M_{\odot}\,yr^{-1}$). The study brings out the importance of multiwavelength SED

analysis and simultaneous FUV and NUV observation to get a better estimation of the accretion luminosity and accretion rate of TTSs.

Comparing the UV color with the IR color, we notice that stars with a higher IR color excess, i.e., the presence of a substantial amount of material in the disk, appear redder in the (FUV–NUV) color, and vice versa. This suggests that stronger FUV emission might have caused the depletion of the gas in the disk. However, a study with a large number of samples is required for a better understanding of this relation.

Acknowledgments

This publication uses UVIT data from the AstroSat mission of the ISRO, archived at the Indian Space Science Data Centre (ISSDC). The UVIT project is a result of collaboration between IIA, Bengaluru; IUCAA, Pune; TIFR, Mumbai; several centers of ISRO; and CSA. This publication uses UVIT data processed by the payload operations center by the IIA. We thank the staff of IAO, Hanle, and CREST, Hosakote, that made these observations possible. The facilities at IAO and CREST are operated by the Indian Institute of Astrophysics, Bangalore. P. K.N. acknowledges TIFR's postdoctoral fellowship. P.K.N. also acknowledges support from the Centro de Astrofisica y Tecnologias Afines (CATA) fellowship via grant Agencia Nacional de Investigacion y Desarrollo (ANID), BASAL FB210003.

ORCID iDs

Prasanta K. Nayak https://orcid.org/0000-0002-4638-1035
Mayank Narang https://orcid.org/0000-0002-0554-1151
P. Manoj https://orcid.org/0000-0002-3530-304X
Uma Gorti https://orcid.org/0000-0002-3311-5918
Annapurni Subramaniam https://orcid.org/0000-0003-4612-620X
Chayan Mondal https://orcid.org/0000-0003-4531-0945

References

Alcala, J. M., Covino, E., Franchini, M., et al. 1993, A&A, 272, 225
Allard, F., Homeier, D., & Freytag, B. 2011, in ASP Conf. Ser. 448, 16th Cambridge Workshop on Cool Stars, Stellar Systems, and the Sun, ed. C. Johns-Krull, M. K. Browning, & A. A. West (San Francisco, CA: ASP), 91
Babusiaux, C., Fabricius, C., Khanna, S., et al. 2023, A&A, 674, A32
Bai, X.-N., Ye, J., Goodman, J., & Yuan, F. 2016, ApJ, 818, 152
Bailer-Jones, C. A. L., Rybizki, J., Fouesneau, M., Demleitner, M., & Andrae, R. 2021, AJ, 161, 147
Barrado y Navascués, D., & Martín, E. L. 2003, AJ, 126, 2997
Bayo, A., Rodrigo, C., Barrado Y Navascués, D., et al. 2008, A&A, 492, 277
Bianchi, L., Shiao, B., & Thilker, D. 2017, ApJS, 230, 24
Calvet, N., & Gullbring, E. 1998, ApJ, 509, 802
Carrera, D., Gorti, U., Johansen, A., & Davies, M. B. 2017, ApJ, 839, 16
Cui, X.-Q., Zhao, Y.-H., Chu, Y.-Q., et al. 2012, RAA, 12, 1197
Dahm, S. E. 2008, AJ, 136, 521
Duvert, G., Guilloteau, S., Ménard, F., Simon, M., & Dutrey, A. 2000, A&A, 355, 165
Esplin, T. L., & Luhman, K. L. 2019, AJ, 158, 54
Fang, M., van Boekel, R., Wang, W., et al. 2009, A&A, 504, 461
France, K., Schindhelm, E., Bergin, E. A., Roueff, E., & Abgrall, H. 2014, ApJ, 784, 127
Gaia Collaboration, Brown, A. G. A., Vallenari, A., et al. 2021, A&A, 649, A1
Gómez de Castro, A. I., Lopez-Santiago, J., López-Martínez, F., et al. 2015, ApJS, 216, 26
Gorti, U., & Hollenbach, D. 2009, ApJ, 690, 1539
Gras-Velázquez, À., & Ray, T. P. 2005, A&A, 443, 541
Gullbring, E., Hartmann, L., Briceño, C., & Calvet, N. 1998, ApJ, 492, 323
Hartmann, L., Herczeg, G., & Calvet, N. 2016, ARA&A, 54, 135
Henden, A. A., Levine, S., Terrell, D., & Welch, D. L. 2015, AAS Meeting, 225, 336.16
Herbig, G. H., & Bell, K. R. 1988, Third Catalog of Emission-Line Stars of the Orion Population (Santa Cruz, CA: Lick Observatory)
Herczeg, G. J., & Hillenbrand, L. A. 2008, ApJ, 681, 594
Inés Gómez de Castro, A., de la Fuente Marcos, R., Canet, A., et al. 2024, A&A, 681, A72
Ingleby, L., Calvet, N., Herczeg, G., et al. 2013, ApJ, 767, 112
Ingleby, L., Calvet, N., Hernández, J., et al. 2011, AJ, 141, 127
Kenyon, S. J., Brown, D. I., Tout, C. A., & Berlind, P. 1998, AJ, 115, 2491
Lada, C. J. 1987, in IAU Symp. 115, Star Forming Regions, ed. M. Peimbert & J. Jugaku (Cambridge: Cambridge Univ. Press), 1
Magnier, E. A., Schlafly, E. F., Finkbeiner, D. P., et al. 2020, ApJS, 251, 6
Manara, C. F., Robberto, M., Da Rio, N., et al. 2012, ApJ, 755, 154
Martín, E. L. 1998, AJ, 115, 351
Mathew, B., Manoj, P., Narang, M., et al. 2018, ApJ, 857, 30
McClure, M. K., Calvet, N., Espaillat, C., et al. 2013, ApJ, 769, 73
Meyer, M. R., Calvet, N., & Hillenbrand, L. A. 1997, AJ, 114, 288
Narang, M., Manoj, P., Tyagi, H., et al. 2023, JApA, 44, 92
Nayak, P. K., Narang, M., Manoj, P., et al. 2024, arXiv:2403.19478
Nayak, P. K., Narang, M., Puravankara, M., et al. 2023, JApA, 44, 83
Owen, J. E., & Wu, Y. 2016, ApJ, 817, 107
Pascucci, I., Ricci, L., Gorti, U., et al. 2014, ApJ, 795, 1
Pecaut, M. J., & Mamajek, E. E. 2013, ApJS, 208, 9
Postma, J. E., & Leahy, D. 2017, PASP, 129, 115002
Rebassa-Mansergas, A., Solano, E., Jiménez-Esteban, F. M., et al. 2021, MNRAS, 506, 5201
Schneider, P. C., Günther, H. M., & France, K. 2020, Galax, 8, 27
Skrutskie, M. F., Cutri, R. M., Stiening, R., et al. 2006, AJ, 131, 1163
Stetson, P. B. 1987, PASP, 99, 191
Subramaniam, A., Tandon, S. N., Hutchings, J., et al. 2016, Proc. SPIE, 9905, 99051F
Tandon, S. N., Hutchings, J. B., Ghosh, S. K., et al. 2017a, JApA, 38, 28
Tandon, S. N., Postma, J., Joseph, P., et al. 2020, AJ, 159, 158
Tandon, S. N., Subramaniam, A., Girish, V., et al. 2017b, AJ, 154, 128
Ulrich, R. K. 1976, ApJ, 210, 377
Valenti, J. A., Fallon, A. A., & Johns-Krull, C. M. 2003, ApJS, 147, 305
Vogt, S. S., Allen, S. L., Bigelow, B. C., et al. 1994, Proc. SPIE, 2198, 362
White, R. J., & Basri, G. 2003, ApJ, 582, 1109
Yang, H., Herczeg, G. J., Linsky, J. L., et al. 2012, ApJ, 744, 121